PCCP

ROYAL SOCIETY
OF CHEMISTRY

Check for updates

The N(^{4}S) + O$_2$(X$^3\Sigma_g^-$) ↔ O(^{3}P) + NO(X$^2\Pi$) reaction: thermal and vibrational relaxation rates for the ^{2}A′, ^{4}A′ and ^{2}A″ states†

Juan Carlos San Vicente Veliz, [iD] [a] Debasish Koner, [iD] [a] Max Schwilk,[a]
Raymond J. Bemish[b] and Markus Meuwly [iD] *[a]

The kinetics and vibrational relaxation of the N(^{4}S) + O$_2$(X$^3\Sigma_g^-$) ↔ O(^{3}P) + NO(X$^2\Pi$) reaction is investigated over a wide temperature range based on quasiclassical trajectory simulations on 3-dimensional potential energy surfaces (PESs) for the lowest three electronic states. Reference energies at the multi reference configuration interaction level are represented as a reproducing kernel and the topology of the PESs is rationalized by analyzing the CASSCF wavefunction of the relevant states. The forward rate matches one measurement at 1575 K and is somewhat lower than the high-temperature measurement at 2880 K whereas for the reverse rate the computations are in good agreement for temperatures between 3000 and 4100 K. The temperature-dependent equilibrium rates are consistent with results from JANAF and CEA results. Vibrational relaxation rates for O + NO(ν = 1) → O + NO(ν = 0) are consistent with a wide range of experiments. This process is dominated by the dynamics on the ^{2}A′ and ^{4}A′ surfaces which both contribute similarly up to temperatures $T \sim$ 3000 K, and it is found that vibrationally relaxing and non-relaxing trajectories probe different parts of the potential energy surface. The total cross section depending on the final vibrational state monotonically decreases which is consistent with early experiments and previous simulations but at variance with other recent experiments which reported an oscillatory cross section.

1 Introduction

Reactions involving nitrogen and oxygen play important roles in combustion, supersonic expansions, hypersonics, and in atmospheric processes. A particularly relevant process, which is part of the so-called Zeldovich process[1] are the (NO + O/O$_2$ + N) and (NO + N/N$_2$ + O) reactions[2,3] that describe the oxidation of nitrogen. In the forward direction, the reaction also generates reactive atomic oxygen. These reactions, together with a range of other atom plus diatom and diatom plus diatom reactions form the core of the 5- and 11-species model used in hypersonics.[4] At high temperatures ($\sim$20 000 K), as present in thin regions of shock layers created at hypersonic speed flight,[5] the reactive chemical processes can become very complex. This complexity is in part due to a significant degree of non-equilibrium. The lack of experimental information on the kinetics at these high temperatures makes numerical simulations for

reaction cross sections as well as reaction and vibrational relaxation rates a very valuable source of information for characterizing hypersonic flow.

There is also much interest in correctly describing the vibrational distribution of the NO molecules after reactive or nonreactive collisions with atomic oxygen for atmospheric processes. The infrared emission of nitric oxide is one of the main tracers to follow and characterize the energy budget in the upper atmosphere.[6] This emission arises from relaxation of vibrationally excited NO after collisional excitation with atomic oxygen. This relaxation process has also been implicated in nighttime cooling of the thermosphere, above $\sim$100 km. Furthermore, nitric oxide is also formed *in situ* and used as a tracer for combustion and in hypersonic flows where it is commonly observed by Laser Induced Fluorescence (LIF).

Previous studies included experimental and computational characterizations of the reaction dynamics and final state distributions of the products. Using a pulsed beam of energetic nitrogen atoms at 8 km s^{-1} interacting with thermal oxygen under single collision conditions to mimic velocities seen in low earth orbit, the distribution of vibrationally excited NO and state specific reaction cross sections for N + O$_2$ → NO + O were determined.[7] The analysis showed an oscillatory behaviour of

[a] *Department of Chemistry, University of Basel, Klingelbergstrasse 80,*
   CH-4056 Basel, Switzerland. E-mail: m.meuwly@unibas.ch
[b] *Air Force Research Laboratory, Space Vehicles Directorate, Kirtland AFB,*
   New Mexico 87117, USA

† Electronic supplementary information (ESI) available. See DOI: 10.1039/c9cp06085e
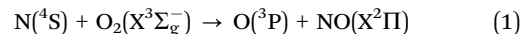
the cross section with increasing final vibrational state, with minima at $\nu = 3$ and $\nu = 6$, with an uncertainty of a factor of two. An even earlier experiment,[8] using saturated multiphoton ionization spectroscopy, measured the NO product ground-state distribution, reporting a difference in the cross sections between odd ($\nu = 1, 3, 5$) and even ($\nu = 0, 2, 4, 6$) final vibrational levels.

From the perspective of computer based simulations[9–11] the vibrational state-dependent cross sections have been calculated using a variety of potential energy surfaces (PESs). In all of these computational studies, the maximum of the final state vibrational cross section is found to be at $\nu = 1$[9] or at $\nu = 2$[10,11] with no notable oscillation. One PES for the $^2A'$ state used a fit[10] to electronic structure calculations at the complete active space SCF (CASSCF) level followed by multireference contracted configuration interaction and a modified Duijneveldt (11s6p) basis set.[12] Another PES was based on 1250 (for the $^2A'$) and 910 ($^4A'$) CASPT2 calculations and fitted to an analytical function.[13] Such an approach was also used for the $^2A''$ state.[14] This was followed by a PESs for the $^2A'$ state using a diatomics in molecules (DIM) expansion with the two-body terms based on extended Hartree–Fock calculations.[15] Then, a 2-dimensional PES with the NO bond length fixed at its equilibrium value of 2.176 a_0 was determined at the icMR-CI+Q/cc-pVQZ level of theory and represented as a cubic spline.[16] This work also presented a PES for the $^2A''$ state. More recently, a double many body expansion fit to 1700 points at the MRCI/aug-cc-VQZ level of theory for the $^2A''$ state was carried out.[17] In addition, quasi classical trajectory (QCT) calculations[2,9,13,18] have been reported for the temperature dependent rate for the $N(^4S) + O_2 \rightarrow NO + O$ and its reverse reaction using different PESs.
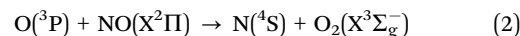
Another important process is the energy transfer following the collision of vibrationally excited NO with oxygen atoms ($O_A + NO_B \rightarrow O_A + NO_B$) or ($O_A + NO_B \rightarrow O_B + NO_A$) to yield NO in its ground vibrational state. Using 355 nm laser photolysis of a dilute mixture of NO_2 in argon, the experiment[3] reports a vibrational relaxation rate of: $k_{\nu=1 \rightarrow 0} = 2.4 \pm 0.5(10^{-11})$ cm^3 s^{-1} at a temperature of $T = 298$ K. Later, QCT simulations[19] reported a value of $k_{\nu=1 \rightarrow 0} = 2.124 \pm 0.73(10^{-11})$ cm^3 s^{-1} at $T = 298$ K which is close to the experimentally reported rate. Another experiment[20] used a continuous wave microwave source to form O atoms combined with photolysis of trace amounts of added NO_2 to generate vibrationally excited NO. This experiment found a rate of $k_{\nu=1 \rightarrow 0} = 4.2 \pm 0.7(10^{-11})$ cm^3 s^{-1} at $T = 295$ K which is larger by 75% compared with the earlier experiments.[3] Quite recent QCT simulations using again the DIM-based PES[15] mentioned above reported a rate of $k_{\nu=1 \rightarrow 0} = 4.34 \pm 0.7(10^{-11})$ cm^3 s^{-1} at $T = 298$ K from QCT simulations[21] which used the empirical DIM PES for the $^2A'$ ground state[15] and a more recent, MRCI-based fitted PES for the $^2A''$ state.[17]

Given the rather heterogeneous situation for the quality of the existing PESs for studying the $N(^4S) + O_2(X^3\Sigma_g^-)$ reaction and the vibrational relaxation of NO, the present work determines fully dimensional PESs using a consistent methodology to represent the 3 lowest electronic states, $^{2,4}A'$ and $^2A''$ as well as to evaluate the cross sections for the (forward)

$$N(^4S) + O_2(X^3\Sigma_g^-) \rightarrow O(^3P) + NO(X^2\Pi) \qquad (1)$$

and (reverse)

$$O(^3P) + NO(X^2\Pi) \rightarrow N(^4S) + O_2(X^3\Sigma_g^-) \qquad (2)$$

reaction. All three states are energetically accessible in the hypersonic regime, *i.e.* at temperatures up to 20 000 K. Experimentally, cross sections and rates for the forward and reverse reactions have been measured and experimental data for vibrational relaxation rates for temperatures up to ~3000 K are available[3,7,8,20,22,23] which serve as benchmarks for the present work.

In the following, the calculation and representation of the asymptotic PESs for the three electronic states and the two channels are described. These are combined to a set of fully-dimensional, reactive PESs which are suitable for quasiclassical trajectory simulations from which cross sections, reaction rates and rates for vibrational relaxation can be determined. The results of the simulations are discussed in the context of the limits of errors in the simulations and comparisons with available experimental data. Finally, the basis of the observables is discussed at an atomistic level, based on analyzing the trajectories.

2 Computational methods

This section presents the generation and representation of the potential energy surfaces and the methodologies for the quasi-classical trajectory (QCT) simulations and their analysis. All PESs are computed at the multi reference CI (MRCI) level of theory together with large basis sets. These are then exactly represented using the reproducing kernel Hilbert space (RKHS) approach. The quality of the representation is then checked using additional MRCI calculated points.

2.1 The $^2A'$, $^2A''$ and $^4A'$ potential energy surfaces

Ab initio energy calculations were carried out for the $^2A'$, $^2A''$ and $^4A'$ states and a correlation diagram with the asymptotic dissociation states is provided in Fig. S1(ESI†). The energies were computed on a grid defined by Jacobi coordinates (r,R,θ) where r is the separation of the diatomic, R is the distance between the atom and the center of mass of the diatomic and θ is the angle between the two unit vectors $\vec{r}$ and $\vec{R}$. For R the grid included 28 points between 1.4 and 12.0 a_0, the distance r was covered by 20 points between 1.5 and 4.0 a_0 and the angular grid contained 13 angles from a Gauss–Legendre quadrature (169.796°, 156.577°, 143.281°, 129.967°, 116.647°, 103.324°, 90.100°, 76.676°, 63.353°, 50.033°, 36.719°, 23.423°, 10.204°). Such a grid is advantageous for quantum bound state and scattering calculations for which highly accurate angular integrals are required. In the RKHS scheme, the angular grid $\in [0,180°]$ is mapped onto the interval $[0,1]$, see below. This transformation leads to a denser grid near the end points (*i.e.* 0° or 180°) and evenly spaced in between. Thus, with this

3928 | *Phys. Chem. Chem. Phys.*, 2020, **22**, 3927–3939

This journal is © the Owner Societies 2020

grid RKHS also performs well near 0° or 180° in the present work as demonstrated below.

In order to consistently describe all relevant states and avoid numerical instabilities due to closely-lying states of the same symmetry, state-averaged CASSCF[24–27] calculations including the two lowest states of each symmetry (two spin symmetries and two spatial symmetries) were carried out. For this, the full valence orbital space was included in the active space. A subsequent internally contracted MRCISD[28,29] (referred to as MRCI+Q in the following) calculation including Davidson correction[30] of the lowest state for each symmetry then was used to include dynamical electron correlation contributions at a high order level. The augmented Dunning-type correlation consistent polarize triple zeta (aug-cc-pVTZ)[31] basis set is used in this work. All electronic structure calculations are done with the Molpro-2019.1[32] software package. For each of the electronic states, *ab initio* energy calculations have been performed for total 7280 points for the NO + O channel and 3920 (including symmetry) points for the OO + N channel, *i.e.* overall ∼11 000 points which is more than 5 times more reference calculations compared with previous efforts for the same system and at a similar level of theory. It is to be noted that electronic structure calculations for a fraction of the geometries at large R and/or r converged to excited states. Those points were excluded from the training energy data set.

For certain geometries ($<0.5\%$) far from the strong interaction region the CASSCF or MRCI calculations did not converge. In these cases, the missing grid points were reconstructed using a 2-dimensional reproducing kernel (R,r) for each θ. This procedure of discriminating possible outliers was necessary before constructing the full dimensional RKHS representation of the PES. The 3-dimensional PES for each channel $V(R,r,\theta)$, is constructed using a reciprocal power decay kernel with $n = 2$ and $m = 6$ for the two radial coordinates and a Taylor spline kernel with $n = 2$ for the angular part.[33] The regularization parameter used was $\lambda = 10^{-18}$. It should be noted that in the present work a regularly spaced grid was used for efficiency reasons but that RKHSs can also be constructed for unstructured grids.[33]

The global, reactive 3D PES $V(r_1,r_2,r_3)$ for an electronic state is constructed by summing the individual PESs for each channel

$$V(r_1, r_2, r_3) = \sum_{j=1}^{3} w_j(r_j) V_j(R, r_j, \theta), \qquad (3)$$

using an exponential switching function with weights

$$w_i(r) = \frac{e^{-(r_i/dr_i)^2}}{\sum_{j=1}^{3} e^{-(r_j/dr_j)^2}}. \qquad (4)$$

Here, dr_i are switching function parameters for the two channels (I) O_2 + N and (II) NO + O. These parameters were optimized by a least squares fit to obtain values of (1.25, 1.11, 1.11) a_0, (1.07, 0.87, 0.87) a_0 and (1.40, 1.35, 1.35) a_0 for the $^2A'$, $^4A'$ and $^2A''$ PESs, respectively.

The global, local minima and transition states between the minima and/or entrance channels supported by the PESs were determined using BFGS minimization and the nudged elastic band method[34] as implemented in the atomic simulation environment (ASE).[35]

The two possible ionic channels for the O + NO product are (i) O^+ + NO^- and (ii) O^- + NO^+. To determine their asymptotic energetics relative to the neutral state, energies have been calculated for the equilibrium geometry of the diatomic ions at the MRCI+Q/aug-cc-pVTZ level of theory. The ionization energy and the electron affinity for the oxygen atom are[36,37] 13.61806 eV and[36,38] −1.4610 eV, respectively. Hence, the two ionic dissociation channels are then 13.79 and 7.66 eV above the neutral O + NO channel, respectively.

2.2 Quasi-classical trajectory simulations

The QCT simulations used in the present work have been extensively described in the literature.[39–42] Here, Hamilton's equations of motion are solved using a fourth-order Runge–Kutta numerical method. The time step was $\Delta t = 0.05$ fs which guarantees conservation of the total energy and angular momentum. Initial conditions for the trajectories are sampled using standard Monte Carlo sampling method.[39] The reactant and product ro-vibrational states are determined following semiclassical quantization. Since the ro-vibrational states of the product diatom are continuous numbers, the states are assigned by rounding to integer values. Two schemes were used (1) histogram binning (HB), *i.e.* rounding values to the nearest integers, or (2) Gaussian binning (GB), which weights each trajectory with a Gaussian shaped function (with a full width at half maximum of 0.1) centered on the integer values.[41,43,44] Here, both schemes were tested and found to yield comparable results. Therefore results obtained from GB are reported in the following.

The state-to-state reaction cross section at fixed collision energy E_c is $\sigma_{v,j \to v',j'}(E_c) = 2\pi \int_0^{b_{max}} P_{v,j \to v',j'}(b; E_c) b \, db$. This integral can be evaluated using Monte Carlo sampling[39] which yields

$$\sigma_{v,j \to v',j'}(E_c) = \pi b_{max}^2 \frac{N_{v',j'}}{N_{tot}}, \qquad (5)$$

where $N_{v',j'}$ is the number of reactive trajectories corresponding to the final state (v',j') of interest, N_{tot} is the total number of trajectories, $P_{v,j \to v',j'} = N_{v',j'}/N_{tot}$ is the probability to observe a particular transition (v,j) → (v',j'), and b_{max} is the maximum impact parameter for which a reactive collision occurs. Here, b_{max} is calculated by running batches of trajectories at different intervals of b. In the present work stratified sampling[39,45] is used to sample the impact parameter $b \in [0 \leq b \leq b_{max}]$. The sampling strategy is described in detail in previous work.[42]

The thermal rate for an electronic state (i) at a given temperature (T) is then obtained from

$$k_i(T) = g_i(T) \sqrt{\frac{8k_B T}{\pi \mu}} \pi b_{max}^2 \frac{N_r}{N_{tot}}, \qquad (6)$$

This journal is © the Owner Societies 2020

Phys. Chem. Chem. Phys., 2020, **22**, 3927–3939 | **3929**

where $g_i(T)$ is the electronic degeneracy factor of electronic state 'i', μ is the reduced mass of the collision system, k_B is the Boltzmann constant, and, depending on the specific process considered, N_r is the number of reactive or vibrationally relaxed trajectories. In the rate coefficient calculations, the initial ro-vibrational states and relative translational energy (E_c) of the reactants for the trajectories are sampled from Boltzmann and Maxwell–Boltzmann distribution at a given T, respectively. The sampling methodology is discussed in detail in ref. 42.

For the forward reaction $(N(^4S) + O_2(X^3\Sigma_g^-) \rightarrow O(^3P) + NO(X^2\Pi))$ the rate $k_+(T)$ is calculated using degeneracies of 1/6 and 1/3 for the $^2A'$ and $^4A'$ states, respectively, whereas for the reverse reaction $(O(^3P) + NO(X^2\Pi) \rightarrow N(^4S) + O_2(X^3\Sigma_g^-))$ the degeneracies are

$$g_{2A'}(T) = \frac{2}{\left(5 + 3 \cdot e^{\frac{-227.8}{T}} + e^{\frac{-326.6}{T}}\right)\left(2 + 2e^{\frac{-177.1}{T}}\right)} \quad (7)$$

and

$$g_{4A'}(T) = \frac{4}{\left(5 + 3 \cdot e^{\frac{-227.8}{T}} + e^{\frac{-326.6}{T}}\right)\left(2 + 2e^{\frac{-177.1}{T}}\right)} \quad (8)$$

The terms in eqn (7) and (8) are the degeneracies of the J or spin states and the exponential parameters 227.8, 326.6 and 177.1 are the energy differences (in units of K) between two neighboring states. The equilibrium constant is then

$$K_{eq}(T) = \frac{k_+(T)}{k_-(T)}. \quad (9)$$

3 Results

3.1 The potential energy surfaces

An overview of the PESs, see Fig. 1, Fig. S2, and Table 1, for all three states investigated ($^2A'$, $^4A'$, and $^2A''$ from bottom to top) is given as 2-dimensional projections with the two asymptotes (N + OO and O + NO) on the left and right columns in Fig. 1, respectively. It should be noted that these representations are all for diatomic separations (O_2 and NO, respectively) at values of critical points (see Fig. S3–S5, ESI†) and therefore do not exhibit all features of the full 3-dimensional PES.

All PESs for OO + N are symmetric with respect to $\theta = 90°$, as expected. For the $^2A'$ state and the O_2 + N dissociation limit the 2d-PES was generated for TS1 in Fig. S3 (ESI†), i.e. for $R^{(OO)} = 2.33$ a_0. The two symmetry related minima are at $R_e^{(NO)} = 3.23$ a_0 and $\theta = 34°$ and $\theta = 146°$, respectively. For the NO + O dissociation limit the PES with $R^{(NO)} = 2.26$ a_0 (corresponding to MIN3 in Fig. S3, ESI†) displays two minima. They are at $(R^{(OO)} = 3.38$ a_0, $\theta = 35°)$ and $(R^{(OO)} = 3.22$ a_0, $\theta = 150°)$.

For the $^4A'$ state the surface for the O_2 + N dissociation limit has $R^{(OO)} = 2.39$ a_0 for TS1 in Fig. S4 (ESI†) and the 2-dimensional PES in Fig. 1 has the minimum at $R^{(NO)} = 3.19$ a_0 with $\theta = 56°$ and $\theta = 124°$, respectively. Conversely, at the NO + O asymptote, the PES is almost purely repulsive for

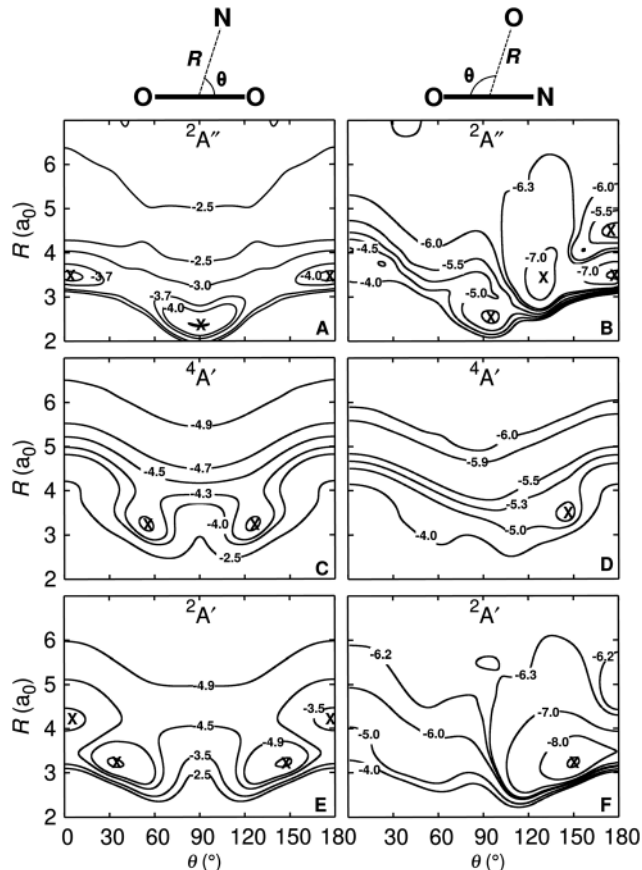Fig. 1 Two-dimensional cuts through the 3-d PES for the OO + N (left) and the NO + O (right) channels. The OO and NO diatomics are at their equilibrium bond lengths of the respective states, see Fig. S3–S5 (ESI†). They are $R^{(OO)} = 2.33$ Å, $R^{(OO)} = 2.39$ Å, $R^{(OO)} = 2.30$ Å, and $R^{(NO)} = 2.26$ Å, $R^{(NO)} = 2.36$ Å, $R^{(NO)} = 2.28$ Å for the $^2A'$, $^4A'$, and $^2A''$ states, respectively, from bottom to top. Specific contours with energies in eV are indicated. The zero of energy is for dissociation into atomic fragments $O(^3P) + O(^3P) + N(^4S)$. The symbols indicate the minima discussed in the text and the definition of the coordinates is given on top of the figure. For the NO + O asymptote the OON geometry corresponds to $\theta = 0$ whereas ONO has $\theta = 180°$.

$R^{(NO)} = 2.36$ a_0 (TS2 in Fig. S4, ESI†). In Jacobi coordinates, a faint minimum is at $(R^{(OO)} = 3.48$ a_0, $\theta = 146°)$.

Finally, for the $^2A''$ state the 2-dimensional PES is reported for $R^{(OO)} = 2.30$ a_0 in the OO + N channel (TS1 in Fig. S5, ESI†). It exhibits two minima at $(R^{(NO)} = 2.36$ a_0, $\theta = 90°)$, and $(R^{(NO)} = 3.55$ a_0, $\theta = (0,180)°)$. At the NO + O asymptote the PES has multiple minima, see Fig. 1. For $R^{(NO)} = 2.28$ a_0 they are at $(R^{(OO)} = 3.69$ a_0, $\theta = 0°)$, $(R^{(OO)} = 2.53$ a_0, $\theta = 95°)$, $(R^{(OO)} = 3.28$ a_0, $\theta = 128°)$, and $(R^{(OO)} = 3.50$ a_0, $\theta = 180°)$.

All minima and transition states together with their connectivities on the 3d PES are given in the ESI,† see Fig. S3–S5 and the geometries and relative energies of the stationary and transition states are summarized in Table 1. All these geometries were determined on the mixed PESs. For comparison, the minima were also determined on the $^2A''$ PES for the NO + O asymptote. The three minima on the unmixed PES are at (MIN1: $r_{OO} = 2.88$ a_0, $r_{NO} = 2.61$ a_0, and an angle 66.8°) with

3930 | Phys. Chem. Chem. Phys., 2020, 22, 3927–3939

This journal is © the Owner Societies 2020

Table 1 Minima (MINi) and transition states (TSi) were calculated using the Nudged Elastic Band (NEB)[34,46] method. Equilibrium distances in a_0, angle in degree for $\angle$(NOO) and $^a\angle$(ONO), and energies ΔE_1 (in eV) with respect to the N + O + O asymptote and ΔE_2 (in kcal mol^{-1}) relative to the N + O$_2$ limit, except for ^{b}(with respect to the global minimum), and ^{c}(relative to the O + NO limit) to compare with the literature. For the energy level diagram and the connectivities, see Fig. S3–S5 (ESI)

^{2}A$'$	$R_e^{(NO)}$	R_e^{OO}	$\angle$ NOO	ΔE_1	ΔE_2	ΔE_2^{13}
MIN1	2.27	2.58	130.4	−5.78	−18.34	−28.50
TS1	3.46	2.33	112.1	−4.64	8.07	6.87
TS2	2.20	2.86	134.1	−5.71	−16.82	−27.42
TS3	2.19	4.63	90.7	−6.29	−30.12	−34.26
MIN2	2.18	4.51	121.1	−6.33	−31.10	−37.64
MIN3	2.26	4.17	22.9	−9.46	−103.20	−108.68

^{4}A$'$	$R_e^{(NO)}$	R_e^{OO}	$\angle$ NOO	ΔE_1	ΔE_2	ΔE_2^{13}
MIN1	2.65	2.60	104.0	−4.69	6.67	5.43
TS1	3.26	2.39	108.0	−4.33	15.01	12.74
TS2	2.36	3.07	103.0	−4.68	8.75	7.81

^{2}A$''$	$R_e^{(NO)}$	R_e^{OO}	$\angle$ NOO	ΔE_1	ΔE_2	ΔE_2^{17}
MIN2	2.23	4.06	107.5^a	−7.37	−111.79	−113.95
TS1	3.96	2.30	111.7	−2.48	0.93	0.63
TS2	4.35	2.31	30.8^a	−2.44	1.95	2.07
TS3	2.57	4.35	80.2^a	−5.54	−69.61	−77.81
TS4	2.42	3.99	109.4^a	−7.22	−108.34	−113.14
TS5	2.39	4.31	130.2^a	−6.78	18.60^b	32.25^b
MIN1	2.61	2.88	67.1^a	−6.16	−83.93	−85.59
MIN3	2.28	4.56	180.0^a	−7.58	−29.06^c	−38.41^c

an energy difference of ΔE = 0.62 kcal mol^{-1}, (MIN2: r_{OO} = 4.09 a_0, r_{NO} = 2.21 a_0, and an angle 107.3°, ΔE = 0.55 kcal mol^{-1}), and (MIN3: r_{OO} = 4.56 a_0, r_{NO} = 2.28 a_0, and an angle 180°, ΔE = 0.005 kcal mol^{-1}). Several paths which include a number

of minima and transition states can be found on the ^{2}A$'$ and ^{2}A$''$ PESs for the forward and reverse reaction while both reactions follow rather simple paths on the ^{4}A$'$ PES. It is worthwhile to note that there are no crossings between the ^{2}A$'$ and ^{2}A$''$ PESs as well as between ^{2}A$'$ and ^{4}A$'$ electronic states which differs from, *e.g.*, the [CNO]-system.[42] For collinear geometries they are, however, degenerate from which a Renner–Teller (rovibronic) coupling may potentially arise but is expected to be of minor significance.

One-dimensional cuts along the O$_2$ + N and NO + O coordinates for constant angle θ for the three different electronic states are reported in Fig. 2. All angular cuts correspond to off-grid points, *i.e.* data not explicitly used in generating the RKHS. Therefore, the RKHS energies (solid lines) are predictions and are found to compare well with the true energies calculated at the MRCI+Q/aug-cc-pVTZ level of theory. Nevertheless, for a few points on the θ = 175.0° cut around $R \sim 4\,a_0$ for the ^{2}A$'$ state (see Fig. 2A) the RKHS-predicted energies differ slightly from the true energies.

The quality of all three PESs for both, on- and off-grid points is reported in Fig. S6 (ESI†) as correlation plots. The correlation between the reference (*ab initio* energies) and RKHS energies ranges from R^2 = 0.9996 to 0.9999 for grid points and from R^2 = 0.9992 to 0.9997 for off-grid points for the three electronic states. The corresponding root mean squared errors for the on-grid points range from 0.022 to 0.043 eV and off-grid points from 0.033 to 0.057 eV. It should be noted that all the RKHS energies are evaluated on the mixed, fully reactive PES, see eqn (3). The agreement between reference and RKHS energies is even better if the channels are considered separately.

To rationalize the observed topology of the NO + O channel of the MRCI+Q PES (Fig. 1 panels B, D, and F), the orbital
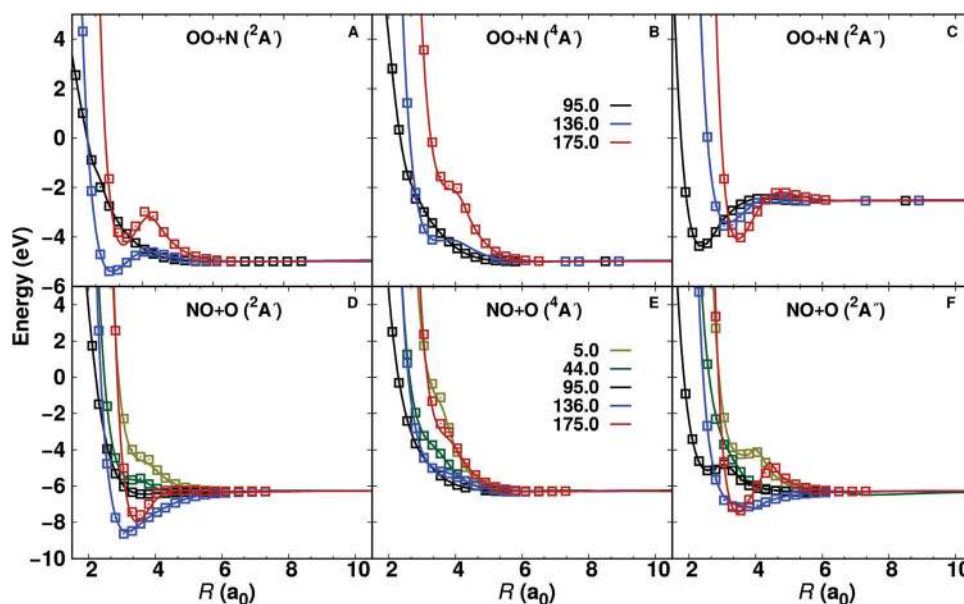

Fig. 2 Quality of the RKHS representation of the 3d PESs at off-grid points. The MRCI+Q/aug-cc-pVTZ reference energies (open symbols) and the RKHS interpolated energies (lines) for the ^{2}A$'$, ^{4}A$'$ and ^{2}A$''$ for the OO + N (top, $r^{(OO)}$ = 2.30 a_0) and NO + O (bottom, $r^{(NO)}$ = 2.19 a_0) channels are reported. In all cases the shape of the PES is correctly captured and the deviations at off-grid points are remarkably small except for one single point in the OO + N (^{2}A$'$) channel.

diagram of the natural orbitals as obtained from the CASSCF calculations are analyzed. Fig. 3 shows the evolution of the natural orbitals and the energies for $R = 3.4$ a_0 and $r_{NO} = 2.183$ a_0 (equilibrium NO separation) with varying values of θ. Only natural orbitals with significant change in occupation number are shown along the path. Fig. S8 (ESI†) shows a complete MO diagram of the valence space. The dominant configurations for the lowest $^2A'$ and $^2A''$ states are indicated in the MO diagrams, and an illustration of all main configurations along the path is given in Fig. S7 (ESI†). The cut qualitatively includes most of the stationary states of the 2-dimensional PESs of the NO + O channel (see Fig. 1 and Fig. S6, ESI†). For the linear structures (Fig. 3A) two perpendicular π_3-systems arise with one electron in an antibonding π_3^* orbital. The bonding orbital of the π-system shows a more equal contribution from all three atomic centers for the linear ONO structure than for the linear OON structure, making the bonding situation more stable in this case (see Fig. S8, ESI†). Bending of the linear structures leads to a transformation of the in-plane antibonding orbitals of the π-system ("a" in Fig. 3A) into a non-bonding p-orbital on the oxygen at $\theta = 90°$. The two non-bonding orbitals of the linear π-systems transform also into p-orbitals on the oxygen. Hence, at $\theta = 90°$ three natural orbitals close in energy with mostly p-orbital contribution on the oxygen atom arise. Their energy fine-ordering depends on the amount of residual

antibonding character they bear. However, the out-of-plane antibonding orbital of the linear π-systems (b in Fig. 3A) transforms into an antibonding π^* NO-orbital upon bending. Finally, the antibonding orbital with dominant σ^*-character for the linear structures ("c" in Fig. 3A) also transforms into an antibonding π^* NO-orbital at $90°$, considerably lowering its orbital energy. The fine-ordering of the two π^* NO-orbitals again depends upon their remaining additional antibonding character. Thus, for a T-shaped structure ($\theta = 90°$) the quasi-degeneracies lead to a large number of configurations with similar energy and lead to small energy differences for the eight states included in the CASSCF wavefunction (see Fig. 3B).

Two additional interesting observations on the NO + O channel can be made from the MO diagram: (1) No stable covalent bonding between the oxygen and the N–O fragment in the T-shaped structure is observed at the CASSCF level of theory. This explains the almost fully repulsive character of the NO + O channel along R for θ close to $90°$ (cf. Fig. 2). (2) Upon bending, the in-plane π_3^* orbital ("a" in Fig. 3A) significantly lowers its energy. As the π_3^* orbitals are partially occupied for the linear structures, bending makes lower energy configurations accessible, yielding minima on the PESs of the NO + O channel for slightly bent structures (cf. Fig. 1). This classifies as a Jahn–Teller distortion.

The CASSCF energies for the eight states along the bending coordinate are shown in Fig. 3B. In the following significant features (i to ix) of the PESs are discussed. For the linear structures (OON ($\theta = 0$) and ONO ($\theta = 180°$)) the orbital degeneracy leads to $^{2,4}A'$ and $^{2,4}A''$ lowest states of equal energy (see points i to iv in Fig. 3B). These conical intersections are symmetry-required and go along with Jahn–Teller distortions. The angle θ is the only degree of freedom that lifts the degeneracy. Bending away from the linear geometry leads to an approach and avoided crossing of the $1^2A''$ and $2^2A''$ states ($\theta = 30°$, point v), each of which is described by one dominant configuration outside the crossing region. A similar observation is made for the $1^2A'$ and $2^2A'$ states ($\theta = 50°$, point vi). The $1^2A'$ state has a strong multi-reference character with various configurations contributing in an extended region $50° \leq \theta \leq 100°$. As indicated in Fig. 3A, the quasi degeneracies in the T-shaped structures gives rise to a large number of configurations with similar energies and to seven states within 0.9 eV for $\theta = 90°$ (point vii). The characteristics of points vii and ix can be described along the same lines as for points vi and v, respectively. The full and detailed analysis of changes in configurations of the states along the path is given in Fig. S7 (ESI†). It is noted that the two lowest ^4A states do not show an avoided crossing and have each one dominant configuration along θ. This explains the rather simple topology of the $1^4A'$ PES in Fig. 1. The inset in Fig. 3 amplifies the subtle changes in state order around $\theta = 90°$. Various additional avoided crossings can be observed (their analysis is given in Fig. S7, ESI†).

For the production calculations eight states are included in the CASSCF reference wave function. Exploratory calculations were also run with 12 states in the state-averaging. For the three lowest states ($^{2,4}A'$ and $^2A''$) using 8 or 12 states leads to the same bending
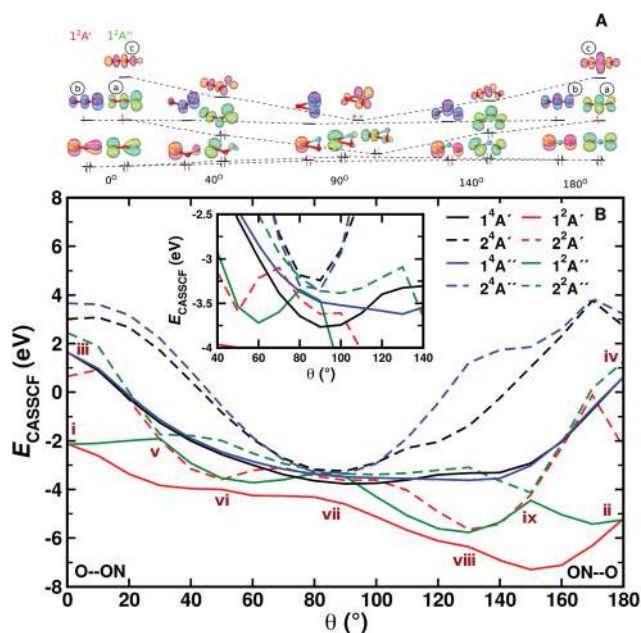

Fig. 3 Panel A: MO diagram of NO_2 for the doublet ground state for varying values of θ. The dominant configurations at selected angles are shown for the lowest $^2A'$ and $^2A''$ states (in black occupations occurring for both states, state-specific orbital occupations are colour-coded). An asterisk indicates significant (additional) occupation of an orbital due to strong electron correlation. Details for each of the states are provided in Fig. S7 (ESI†). Panel B: CASSCF energies in eV relative to separated atoms. The inset shows details of the states around the T-shaped geometry. Features i through ix are discussed in the text. See also Fig. S9 (ESI†) for MRCI energies. Orbital visulaization was done with IboView.[47]

3932 | Phys. Chem. Chem. Phys., 2020, 22, 3927–3939

This journal is © the Owner Societies 2020

curves, see Fig. S9 (ESI†). Also, the topography of the bending curves is very similar from CASSCF and MRCI+Q calculations (Fig. S10, ESI†). The sextet states were not included as they are expected to be repulsive (see Fig. S1, ESI†) which is of little relevance to the thermal and vibrational relaxation rates considered next.

3.2 Thermal rates and reaction cross sections

Thermal rates for the forward $(N(^4S) + O_2(X^3\Sigma_g^-) \rightarrow O(^3P) + NO(X^2\Pi))$ and reverse $(O(^3P) + NO(X^2\Pi) \rightarrow N(^4S) + O_2(X^3\Sigma_g^-))$ reactions are determined between 300 and 20 000 K. A total of 50 000 trajectories was calculated at each temperature for each reaction on each electronic states. The individual contributions of the $^2A'$ and $^4A'$ states are reported in Fig. 4 panels A and B. The forward rates are about one order of magnitude higher than the reverse rates for both electronic states. Comparison with previous calculations[13] (see Fig. S11, ESI†) shows that for both states and both directions they differ by a factor of ~ 2 for high temperature. For lower temperature they rather differ by a factor of ~ 5.

Fig. 4C and D show the total rate $k(T)$ for the forward and reverse reaction. The total rate is calculated as the weighted contribution of the $^2A'$ and $^4A'$ surfaces, see eqn (6)–(8). For practical applications, such as "Direct Simulation Monte Carlo" (DSMC) simulations,[57] it is also useful to fit the data to an empirical, modified Arrhenius relationship.

$$k(T) = A \cdot T^n \cdot e^{\left(-\frac{B}{T}\right)} \tag{10}$$

Table 2 Arrhenius 3-parameter model (eqn (10)) for $600 \leq T \leq 20\,000$ K for the forward $(N(^4S) + O_2(X^3\Sigma_g^-) \rightarrow O(^3P) + NO(X^2\Pi))$ and reverse $(O(^3P) + NO(X^2\Pi) \rightarrow N(^4S) + O_2(X^3\Sigma_g^-))$ reaction. A in units of 10^{-14} cm^3 per (s molecule)

Parameter	$^2A'$	Lit.[9]	$^4A'$	Lit.[9]	Total	Lit.[2]	Lit.[13]
Forward							
n	0.83	0.63	0.56	0.97	1.18	1.18	1.60
A	3.58	34.0	117.2	2.31	0.370	0.414	0.014
B [K]	4105	4043	8722	7459	4090	4005	2894
Reverse							
n	0.74	—	0.64	—	0.40	—	1.51
A	1.77	—	12.1	—	190.3	—	0.01
B [K]	19 653	—	23 505	—	24 520	—	19 115

The fitted parameters are given in Table 2. Additional fits for N + O$_2$ on the $^4A'$ state yield[9] $A = 1.41 \times 10^{-14}$ cm^3 per (s molecule), $n = 1.04$, $B = 6112$ K based on VTST data.[13] Fitting of earlier QCT data[2] yields remarkably similar values to the present results, see Table 2 and blue trace in Fig. 4C, which, however, differ both substantially from a more recent study.[13] Experimental rates at higher temperatures are rare. One study was carried out at 1575 K[49] which is in quite good agreement within typical[56] uncertainties of 25% with the present simulations (Fig. 4C) whereas the rate from an experiment at higher temperature (2880 K)[51] is larger than the rate from the present and earlier[2] simulations by about a factor of two. One possible explanation is that for experiments above $T \sim 2000$ K there is
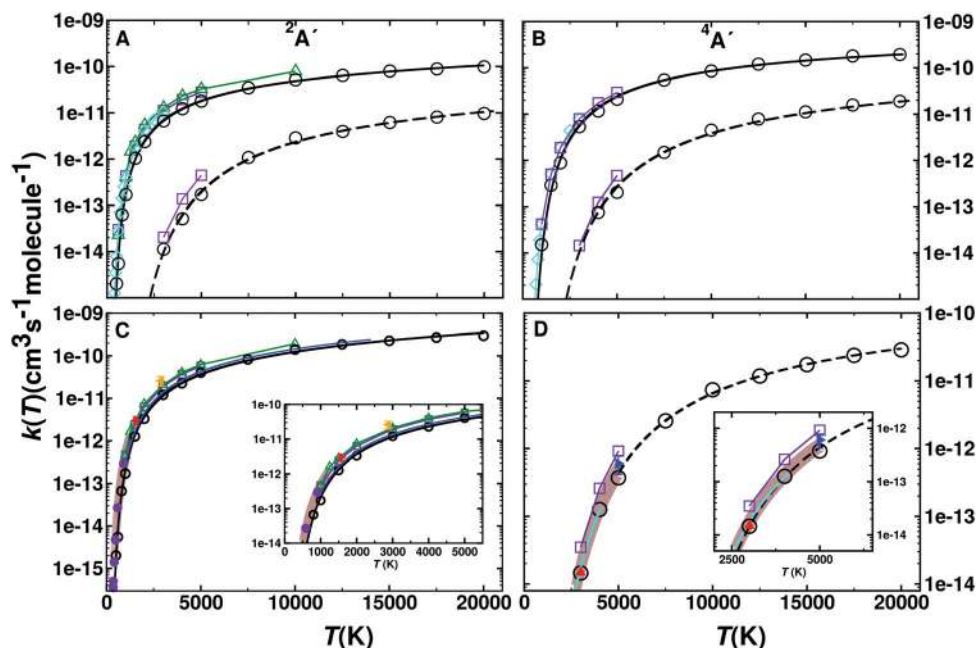

Fig. 4 (top) Rate coefficients for the forward $(N(^4S) + O_2(X^3\Sigma_g^-) \rightarrow O(^3P) + NO(X^2\Pi))$ and reverse $(O(^3P) + NO(X^2\Pi) \rightarrow N(^4S) + O_2(X^3\Sigma_g^-))$ reaction for the $^2A'$ (panel A) and $^4A'$ (panel B) states. Rates for the forward (open circles and solid black line) and reverse (open circles and dashed lines) reaction are given separately. Results from previous computations based on VTST (green open triangle),[9] ICVT (violet open square)[13] and quantum treatments (cyan open diamond)[48] are also shown for comparison. (Bottom) Total rates $k(T)$ for the forward (panel C) and reverse (panel D) reaction from GB (black open circles) and a fit to a 3-parameter Arrhenius model (solid black line, for parameters see Table 2). Results from VTST (green open triangle up),[9] ICVT (violet open square),[13] quantum (cyan open diamond)[48] and evaluation (blue solid line).[2] Experimental values are also reported in Panel C ((red solid right triangle),[49] (magenta solid circle),[50] (orange solid left triangle)[51]) and Panel D ((blue solid right triangle),[52] (red solid triangle up),[53] (blue cyan line)[54]) together with fits to experiment with errors (brown shaded areas in panels C[55] and D[56]).

This journal is © the Owner Societies 2020

Phys. Chem. Chem. Phys., 2020, **22**, 3927–3939 | **3933**

interference between the O + N$_2$ and N + O$_2$ reactions and the analysis required a reaction network both of which introduce uncertainties in the rate.[51] For the reverse rate the present simulations accurately describe those measured experimentally.[52,53,56]

The reverse rate (O + NO) in ref. 9 was not determined from QCT simulations but rather by first computing the equilibrium constant $K_{eq}(T)$ according to statistical mechanics and then using $k_-(T) = k_+(T)/K_{eq}(T)$. The Arrhenius values from ref. 9 are $A = 0.114 \times 10^{-14}$ cm^3 per (s molecule), $n = 1.13$, and $B = 19\,200$ K. To the best of our knowledge the present work determined $k_-(T)$ for the first time from QCT simulations.

In addition, the equilibrium constant $K_{eq}(T)$ as defined in eqn (9) is also calculated (see Fig. 5) as it can be compared directly with experimental work. For $K_{eq}(T)$ the present calculations agree favourably with the JANAF and CEA values over the entire temperature range, as can be expected since K_{eq} is also determined from the difference in Gibbs free energy between the initial and final states.

To determine the cross sections depending on the final vibrational state ν', additional simulations were carried out. For this 2×10^5 independent trajectories on each of the three electronic states were run starting from the N + O$_2$ asymptote with a distribution of O$_2$ internal (ν,j) states at 1000 K to follow N(^{4}S) + O$_2$(X$^3\Sigma_g^-$) → O(^{3}P) + NO(X$^2\Pi$)(ν',j). Then, total reaction cross sections for the individual final vibrational states (ν',j) were determined. The cross section as a function of the vibrational level (ν') is reported in Table 3 and compared with previous experimental[7] and theoretical[9] work. Of particular interest is the dependence of σ on the final vibrational state ν' of NO because experimentally, an oscillating total cross section had been found with minima at $\nu' = 3$ and $\nu' = 5$.[7] However, earlier experiments[59,60] report the rate constant for formation of NO for the N + O$_2$ → NO + O reaction for vibrational levels $\nu = 2$–7. Using eqn (6) these rates were converted into cross sections which are monotonically

Table 3 Individual and total cross sections (in Å^2) for the N + O$_2(\nu)$ → NO(ν') + O process as a function of the final vibrational state (ν') at a rovibrational and translational temperature of 1000 K from Gaussian binning. The total cross sections are also compared with experimental results (Exp.)[61] and rates for NO formation (Exp.)[59] converted to cross sections according to eqn (6). Additionally, comparison with other computational work (Lit.).[9–11] is also provided

State ν'	Exp.[61]	Exp.[59]	^{2}A'	^{4}A'	Total	Lit.[10]	Lit.[11]	Lit.[9]
0	—	—	0.17	0.67	0.84	—	0.28	0.50
1	0.49	—	0.16	0.48	0.64	0.37	0.41	0.53
2	0.65	0.37	0.14	0.31	0.45	0.42	0.46	0.48
3	0.20	0.39	0.14	0.22	0.36	0.39	0.44	0.43
4	0.69	0.22	0.12	0.16	0.28	0.36	0.37	0.32
5	0.37	0.16	0.10	0.10	0.20	0.31	0.32	0.26
6	0.20	0.04	0.09	0.07	0.16	0.27	0.28	0.20
7	0.25	0.03	0.07	0.05	0.12	0.23	0.24	0.18

decreasing with ν except for $\nu = 2$.[59] Rates for $\nu = 0$ and $\nu = 1$ were reported to be larger compared to $\nu \geq 2$.[59] A comprehensive comparison of the present results for the cross sections is given in Table 3.

No oscillating behaviour of the cross section was found from the present simulations, see Fig. 6. This finding agrees with previous simulations[9] based on a DIM PES for the ^{2}A' state[15] and a fitted MBE to CASPT2 calculations for the ^{4}A' state.[13] The present calculations find a decaying cross section with higher vibrational state. The individual contributions of the (^{2}A') and (^{4}A') state are calculated in addition to the total contribution which is the weighted sum of the individual states. The previous computational work[9] also used the contribution of both the ^{2}A' and ^{4}A' states and found a small population inversion peaking at $\nu' = 1$. But overall, the findings from both simulation studies are consistent and suggest that the experimental findings[7] should be reconsidered.
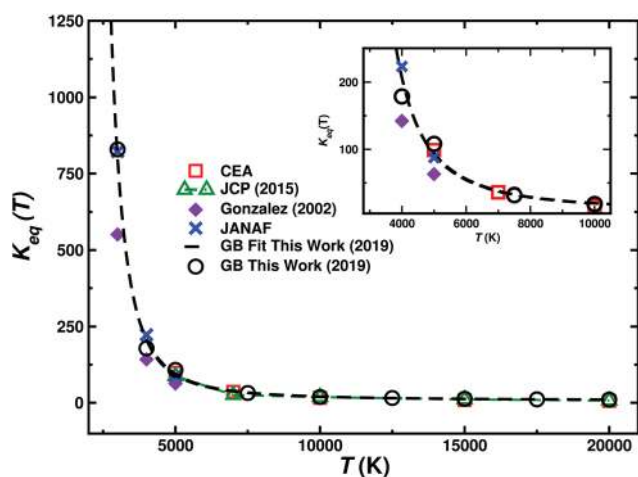

Fig. 5 Equilibrium constant $K_{eq}(T)$. QCT results calculated in this work (circles), fit to a modified Arrhenius model (solid lines) for temperatures between 1000 and 20 000 K. Previous QCT,[58] JANAF tables[23] and Chemical Equilibrium with Application (CEA) results[22] are also included for comparison. The inset shows an enlarged view for lower temperatures.
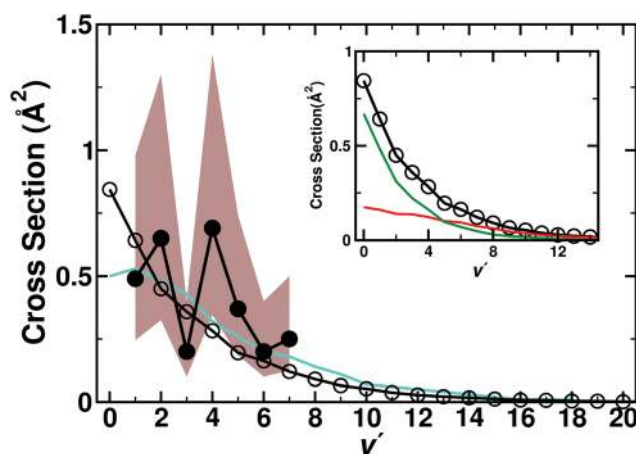

Fig. 6 Vibrational state-dependent, total cross sections (in Å^2) for the N + O$_2(\nu)$ → NO(ν') + O process as a function of the final ν'. Total contribution (^{2}A' + ^{4}A') (open circles and black line) compared with previous computations (turquoise line)[9] and experiment (black solid circles)[7] with error region (brown shaded area) results. The inset reports the individual contributions from the present work for the ^{2}A' (red) and ^{4}A' (green), together with the total cross section.

3934 | *Phys. Chem. Chem. Phys.*, 2020, **22**, 3927–3939

This journal is © the Owner Societies 2020

3.3 Vibrational relaxation

As a third observable reactive (oxygen exchange) and non-reactive vibrational relaxation of $O + NO(\nu = 1) \rightarrow O + NO(\nu = 0)$ was studied on the RKHS PESs for all three electronic states as a function of temperature. As has also been noted in previous work, there are a total of 36 states that can potentially participate in the vibrational relaxation dynamics.[21,62] However, only energetically low-lying states of $^2A'$ and $^2A''$ symmetry have attractive wells. As the efficiency of vibrational relaxation depends on the contact time between the diatomic and the collision partner, only these two states are deemed to be relevant at the temperature considered in this section, which is $T \leq 3000$ K. Such a treatment is also consistent with previous investigations.[21,62] Nevertheless, simulations were also carried out for the $^4A'$ state.

An early experiment[3] determined the rate for $NO(\nu = 1)$ vibrational relaxation by O atoms at room temperature. The vibrationally excited NO and relaxer O atoms were formed using 355 nm laser photolysis of a dilute mixture of NO_2 in an argon bath gas. The reported total rate was $k_{\nu=1 \to 0} = 2.4 \pm 0.5(10^{-11})$ cm^3 s^{-1} at $T = 298$ K. It was argued that this value is 2 to 3 times lower than the generally accepted value of K used in atmospheric modeling.[63,64] Subsequent QCT simulations[19] on the $^2A'$ and $^2A''$ states, find a value of $k_{\nu=1 \to 0}(T = 298$ K$) = 2.124 \pm 0.73(10^{-11})$ cm^3 s^{-1}. It should be noted that the PESs for these two states are based on different approaches. For the $^2A'$ PES it is based on a DIM ansatz[15] whereas the $^2A''$ PES is a MBE fit to CASPT2 calculations.[14] Even earlier calculations using the $^2A'$ PES obtained a somewhat smaller rate of $k_{\nu=1 \to 0}(T = 298$ K$) = 1.7(10^{-11})$ cm^3 s^{-1}.[65]

A more recent experiment[20] used a continuous wave microwave source to generate oxygen atoms, combined with photolysis of trace amounts of added NO_2 to produce vibrationally excited NO. The rate for vibrational relaxation is $k_{\nu=1 \to 0}(T = 295$ K$) = 4.2 \pm 0.7(10^{-11})$ cm^3 s^{-1} which is an increase by 75% compared with the earlier results.[3] Later QCT simulations[21] based on the DIM PES for the $^2A'$ state[15] and a fitted DMBE PES based on 1681 MRCI/AVQZ calculations for the $^2A''$ state[17] report a value of $k_{\nu=1 \to 0}(T = 298$ K$) = 4.34 \pm 0.7(10^{-11})$ cm^3 s^{-1}. Another computational study[62] reported a value of $k_{\nu=1 \to 0}(T = 300$ K$) \sim 5(10^{-11})$ cm^3 s^{-1}.

As to compare with the more recent experiments[20] the individual contributions of the $^2A'$, $^4A'$, and $^2A''$ states towards vibrational relaxation of $O + NO(\nu = 1) \rightarrow O + NO(\nu = 0)$ were determined here. Additionally, the total rate is compared with previous theoretical[19,21] and experimental[3,20] results, see Fig. 7. In particular for low temperature the agreement with the more recent[20] experiments and the only high-temperature experiment (at 2700 K)[66] is noteworthy. The results from the simulations based on high-level, 2-dimensional PESs[16] for the $^2A'$ and $^2A''$ states are also in good agreement with the experiments and the present simulations.

As can be seen in Fig. S12 (ESI†) and Table 4, trajectories run on the $^2A'$ state contribute most to the vibrationally relaxing (VR) rates. Hence, to explore whether and how the process of vibrational relaxation ($O + NO(\nu = 1) \rightarrow O + NO(\nu' = 0)$) and sampling of the underlying PES are related, another 25 000 independent trajectories were run for the $^2A'$ state at 530 K.
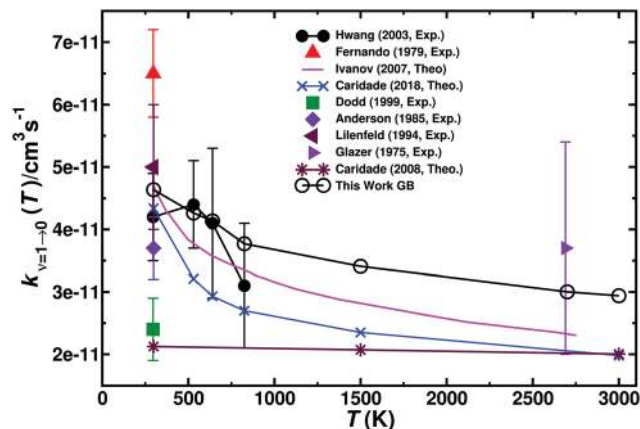

Fig. 7 Total vibrational relaxation rate for $O + NO(\nu = 1) \rightarrow O + NO(\nu = 0)$. The individual contributions of the $^2A'$, $^4A'$, and $^2A''$ states are provided in Fig. S12 (ESI†). Present data from Gaussian binning are open black circles and literature values are the symbols as indicated.[3,16,19–21,63,66–68]

Table 4 Electronic state-dependent vibrational relaxation rates (in units of $10^{11})k_{\nu \to \nu'}$: $O + NO(\nu = 1) \rightarrow O + NO(\nu' = 0)$ for the $^2A'$, $^4A'$ and $^2A''$ states and the total contribution using GB

	298 K	530 K	640 K	825 K	1500 K	2700 K	3000 K
$^2A''$	2.21	1.98	1.82	1.63	1.42	1.13	1.16
$^4A'$	0.00	0.00	0.00	0.00	0.01	0.08	0.12
$^2A'$	2.43	2.28	2.32	2.15	1.98	1.80	1.66
Total	4.64	4.26	4.14	3.77	3.41	3.00	2.94
Exp.[20]	4.2 ± 0.7	4.4 ± 0.7	4.1 ± 1.2	3.1 ± 1.0	—	—	—

Out of those, 5722 relaxed to $\nu' = 0$ whereas for 13 311 trajectories either the internal state of NO was changed to ($\nu' \neq 0, j'$) or O_2 was produced. For the remaining 5967 (nonreactive) trajectories the initial ro-vibrational state is not changed. All the trajectories were saved and rigorous analysis have been carried out to investigate the relaxation process. The opacity function $P(b)$ for relaxing trajectories computed on $^2A'$ PES is reported in Fig. S13 (ESI†).

The probability distributions of different O + NO configurations for different types of trajectories have been computed in (R, θ) space. Structures are included in the computation only if any of the NO bond is within 2.03 to 2.39 a_0 (the turning points for the $\nu = 1$ state of NO are $r_{min} = 2.046$ a_0 and $r_{max} = 2.370$ a_0). Gaussian binning with bin size $\Delta R = 0.1$ a_0 and $\Delta \theta = 3°$ was used and contributions from 2.03 $a_0 < r_{NO} < 2.39$ a_0 are excluded. Individually normalized distributions for relaxing (Fig. 8A) and nonrelaxing (Fig. 8B) trajectories are then projected on an r-relaxed 2D PES. This PES was computed by determining the minimum energy for given (R, θ) with $r \in [2.03, 2.39]$. Such an r-relaxed PES is a more realistic way for this comparison as it also incorporates the varying NO bond length during the dynamics instead of restricting it to one specified value.

Fig. 8 demonstrates that the two families of trajectories sample distinct regions of the interaction potential. The VR trajectories have a high density in the deep potential well area
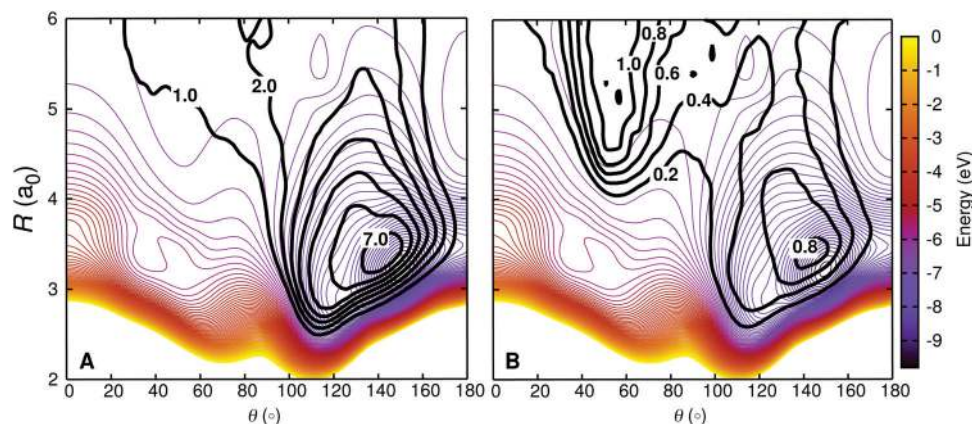
This journal is © the Owner Societies 2020

Phys. Chem. Chem. Phys., 2020, **22**, 3927–3939 | **3935**

Fig. 8 Density trajectory map for the vibrationally relaxing (left) and non-relaxing (right) for O + NO(ν = 1,j) collisions on the ^{2}A′ PES. Vibrationally relaxing trajectories includes both, reactive and non-reactive trajectories, *i.e.* O_A + NO_B → O_B + NO_A and O_A + NO_B → O_A + NO_B, whereas for the non-relaxing trajectories we excluded the trajectories for which the initial ro-vibrational state is not changed. The density map for the trajectories is superimposed on a relaxed 2D RKHS PES (see text for details). The two different classes of trajectories access different regions in configuration space, corresponding to different angular anisotropies.

(dark blue) of the PES and sample mostly $\theta > 90°$ region. This suggests formation of a long lived, tightly bound collision complex. However, the non-relaxing (NR) trajectories spend less time in the potential well region and the density map is rather flat, more uniformly distributed along the angular coordinate with slightly larger sampling in the low-θ region.

To check the initial (before collision) angular dependence of the trajectories and role of long-range anisotropic interactions between the atomic collider and the diatomic target, similar density maps like Fig. 8 have been computed for the VR and NR trajectories only up to the time satisfying the criterion that the sum of the three inter-nuclear distances is less than 9.5 a_0. Those are shown for the NR trajectories in Fig. S14 and for the relaxing in Fig. S15 (ESI†). It can be seen that at a separation of $\sim$8.5 a_0 the distribution $P(\theta)$ already has "structure" for the NR trajectories and in that a large fraction samples the range $\theta \sim 50°$ while the NR trajectories scarcely sample the high-θ region. However, for the relaxing trajectories the distribution is much more even and lacks a specific high-probability characteristic for a particular angle. Since the low-θ region of the PES is repulsive, most of the trajectories are reflected with only changing the rotational state of the NO and resulting NR events. A large fraction of those NR trajectories could not even visit the short-range interaction region ($R < 6.0$ a_0) and they fly by from the target contributing twice (incoming and outgoing trajectories) more in the density map which is obvious in Fig. S14 (ESI†).

In Fig. S16 (ESI†), ten randomly selected VR (red) and NR (black) trajectories from each of the data set plotted in Fig. S14 and S15 (ESI†) are projected on similar 2D PES as in Fig. 8. The dashed lines represent the reactive (oxygen exchange or O_2 formation) trajectories. It can be seen that all VR trajectories sample the potential well region which supports a collision complex. Out of the 10 VR trajectories 3 involve a reactive, oxygen exchange event. The ratio 7 : 3 is representative of all trajectories (3890 : 1832, for relaxing non reactive *vs.* relaxing

reactive trajectories). Thus, oxygen exchange events contribute almost one third to VR. On the other-hand, among the NR trajectories a certain fraction accesses the global minimum of the PES but most of them do not continue beyond $R < 6.0$ a_0 but are reflected at longer R.

The results above suggest that relaxing and non-relaxing trajectories probe different parts of the PES. Hence, in order to be able to realistically describe vibrational relaxation the relevant regions, especially the potential well of the PES, have to be described sufficiently accurately. Fig. S17 (ESI†) reports the same PES together with the positions in (R,θ) for which MRCI+Q calculations were carried out. It can be seen that the relevant regions sampled by vibrationally relaxing and non-relaxing trajectories are covered by the electronic structure calculations. Thus the current PES is expected to provide an accurate description of the interaction potential for relaxation dynamics, which is also supported when comparing the computed rates with experiments.

As indicated above, for a complete description of the process, 36 state would need to be included. Most of them are repulsive and as indicated by the results in Table 4, the repulsive ^{4}A′ state only contributes $\sim$5% to the total relaxation rate at temperatures $T \sim 3000$ K. However, at higher collision energies it is likely that this contribution increases and additional states need to be included. However, as long as the shape of the PESs is not significantly different from that of the ^{4}A′ state, the contributions from all these PESs would enter the total relaxation rate through a statistical factor, similar to the treatment of the thermal rate described in the Methods section.

4 Discussion and conclusions

QCT calculations were carried out on the ^{2}A′, ^{4}A′ and ^{2}A″ electronic states of NO_2 for both, the forward and reverse reaction. The total rates agree favourably with experiment for

3936 | *Phys. Chem. Chem. Phys.,* 2020, **22**, 3927–3939

This journal is © the Owner Societies 2020

the forward and reverse reaction (Fig. 4C and D), except for the experiment for the forward rate at 2880 K for which interference with reactions such as $N_2 + O$ render the analysis more difficult.[51] The T-dependent equilibrium constants are close to those reported in the JANAF tables[23] and to those from results reported in Chemical Equilibrium with Application (CEA).[22] This latter fact suggests that the forward rate $k_+(T)$ is in fact preferred over the single available experimental result at higher temperature (2880 K).[51] Vibrational relaxation rates were computed for the $O + NO(\nu = 1) \rightarrow O + NO(\nu = 0)$ process. Both states, $^2A'$ and $^2A''$, contribute to vibrational relaxation whereas the contribution from the $^4A'$ state is small at low temperature ($k \approx 10^{-14}$) but increases for higher temperatures (Table 4).

For VR to occur, the force on the NO oscillator must act along the chemical bond, not orthogonal to it. Hence, the PES along the $\theta = 0$ and $\theta = 180°$ directions are most relevant to convert translational energy of the oxygen atom into relaxation of the vibrational motion of the NO diatomic, see Fig. 8. As around $\theta = 0$ the PES is repulsive it is primarily the region around $\theta = 180°$ which VR is sensitive to. The present work highlights that different parts of the PESs are probed depending on the observable considered, which can even be demonstrated explicitly. For example, using the DIM PES for the $^2A'$ state for computing the $N + O_2 \rightarrow O + NO$ temperature-dependent rate coefficients together with contributions for the $^4A'$ state from the literature, acceptable agreement with experiment can obtained whereas for the temperature dependent vibrational relaxation the DIM PES finds a T-independent rate (see Fig. 7) which considerably underestimates that reported from experiments.

The fact that different observables provide information about different parts of the PES has already been highlighted for van der Waals complexes. As an example, the morphed PESs for the Ne–HF complex[69] demonstrated that observables from high resolution spectroscopy about the lowest stretching and bending states along the van der Waals coordinate provide sensitive information about the linear Ne–HF approach but no information about the antilinear Ne–FH part of the PES. Hence, it will be interesting to relate the space sampled by trajectories leading to particular final states with specific features such as to better understand what parts of a PES are crucial for reliably characterizing experimental observables from high-level computational studies.

It is expected that the temperature dependence of the rates computed in the present work extrapolate more reliably to higher temperature than the experimental data because, as the collision energy increases, the simulations sample the near vertical repulsive wall of the diatomic, determining its size. As this is an exponentially increasing curve, errors in the exponent will make little difference in the radius that is accessible at a given energy.

The present work uses one of the highest affordable levels of theory for the electronic structure calculations (MRCI+Q) and the validity of their representation as a RKHS is thoroughly tested using a large number of off-grid points. The topology of the PESs could be fully rationalized with an analysis of the

CASSCF wave function of the different states. Being the reference wave function of the MRCI+Q calculation, CASSCF gives a qualitatively correct picture of the relevant wave function characteristics. Investigating the effect of nonadiabatic transitions – as has recently been done for the [CNO] system – will provide additional valuable information in future work.

In summary, the reactive dynamics, thermal rates and vibrational relaxation for the $N(^4S) + O_2(X^3\Sigma_g^-) \leftrightarrow O(^3P) + NO(X^2\Pi)$ reaction on the three lowest potential energy surfaces was studied based on QCT simulations. The results are consistent with most of the available experiments. This provides a solid basis for a molecularly refined picture of vibrational relaxation and extrapolation of thermal rates to higher temperatures relevant at the hypersonic flight regime which can be used for more coarse grained studies such as DSMC simulations.

Conflicts of interest

There are no conflicts to declare.

Acknowledgements

References

1 Y. Zeldovich, The Oxidation of Nitrogen in Combustion Explosions, *Acta Physicochimica U.S.S.R*, 1946, **21**, 577–628.

2 D. Bose and G. V. Candler, Thermal rate constants of the $O_2 + N \rightarrow NO + O$ reaction based on the $^2A'$ and $^4A'$ potential-energy surfaces, *J. Chem. Phys.*, 1997, **107**, 6136–6145.

3 J. A. Dodd, R. B. Lockwood, E. S. Hwang, S. M. Miller and S. J. Lipson, Vibrational relaxation of $NO(\nu = 1)$ by oxygen atoms, *J. Chem. Phys.*, 1999, **111**, 3498–3507.

4 R. Gupta, J. Yos, R. Thompson and K. Lee, A Review of Reaction Rates and Thermodynamic and Transport Properties for an 11-Species Air Model for Cheical and Thermal Nonequilibrium Calculations to 30000 K, *Acta Physicochimica U.S.S.R*, 1946, **21**, 577–628.

5 C. Park, Review of chemical-kinetic problems of future NASA missions. I-Earth entries, *J. Thermophys. Heat Transfer*, 1993, **7**, 385–398.

6 K. Venkataramani, J. D. Yonker and S. M. Bailey, Contribution of chemical processes to infrared emissions from nitric oxide in the thermosphere, *J. Geophys. Res. - Space Phys*, 2016, **121**, 2450–2461.

7   G. Caledonia, R. Krech, D. Oakes, S. Lipson and W. Blumberg, Products of the reaction of 8 km s^{-1} N(^{4}S) and O$_2$, *J. Geophys. Res.: Space Phys.*, 2000, **105**, 12833–12837.

8   I. Winkler, R. A. Stachnik, J. I. Steinfeld and S. M. Miller, Determination of NO (ν = 07) product distribution from the N(^{4}S) + O$_2$ reaction using twophoton ionization, *J. Chem. Phys.*, 1986, **85**, 890–899.

9   P. J. B. S. Caridade and A. J. C. Varandas, Dynamics Study of the N(^{4}S) + O$_2$ Reaction and Its Reverse, *J. Phys. Chem. A*, 2004, **108**, 3556–3564.

10 J. W. Duff, F. Bien and D. E. Paulsen, Classical dynamics of the N(^{4}S) + O$_2$ (X$^3\Sigma_g^-$) + NO(X$^2\Pi$) + O(^{3}P) reaction, *Geophys. Res. Lett.*, 1994, **21**, 2043–2046.

11 B. Ramachandran, N. Balakrishnan and A. Dalgarno, Vibrational rotational distributions of NO formed from N + O$_2$ reactive collisions, *Chem. Phys. Lett.*, 2000, **332**, 562–568.

12 S. Walch and R. Jaffe, Calculated potential surfaces for the reactions: O + N$_2$ → NO + N and N + O$_2$ rightarrow NO + O, *J. Chem. Phys.*, 1987, **86**, 6946–6956.

13 R. Sayós, C. Oliva and M. González, New analytical (^{2}A′, ^{4}A′) surfaces and theoretical rate constants for the N(^{4}S) + O$_2$ reaction, *J. Chem. Phys.*, 2002, **117**, 670–679.

14 M. González, I. Miquel and R. Sayós, Ab initio, VTST, and QCT study of the 1^{2}A″ potential energy surface of the N(^{2}D) + O$_2$(X$^3\Sigma_g$) → O(^{3}P) + NO(X$^2\Pi$) reaction, *J. Chem. Phys.*, 2001, **115**, 8838–8851.

15 A. Varandas, A realistic multi-sheeted potential energy surface for NO$_2$(^{2}A′) from the double many-body expansion method and a novel multiple energy-switching scheme, *J. Chem. Phys.*, 2003, **119**, 2596–2613.

16 M. V. Ivanov, H. Zhu and R. Schinke, Theoretical investigation of exchange and recombination reactions in O(^{3}P) + NO($^2\Pi$) collisions, *J. Chem. Phys.*, 2007, **126**, 054304.

17 V. C. Mota, P. J. S. B. Caridade and A. J. C. Varandas, *Ab Initio*-Based Global Double Many-Body Expansion Potential Energy Surface for the First ^{2}A″ Electronic State of NO$_2$, *J. Phys. Chem. A*, 2012, **116**, 3023–3034.

18 J. C. Castro-Palacio, T. Nagy, R. J. Bemish and M. Meuwly, Computational study of collisions between O(^{3}P) and NO($^2\Pi$) at temperatures relevant to the hypersonic flight regime, *J. Chem. Phys.*, 2014, **141**, 164319.

19 P. J. S. B. Caridade, V. C. Mota, J. R. Mohallem and A. J. C. Varandas, A Theoretical Study of Rate Coefficients for the O + NO Vibrational Relaxation, *J. Phys. Chem. A*, 2008, **112**, 960–965.

20 E. S. Hwang, K. J. Castle and J. A. Dodd, Vibrational relaxation of NO(ν = 1) by oxygen atoms between 295 and 825 K, *J. Geophys. Res.*, 2003, **108**, 1109.

21 P. J. S. B. Caridade, J. Li, V. C. Mota and A. J. C. Varandas, The O + NO(ν) Vibrational Relaxation Processes Revisited, *J. Phys. Chem. A*, 2018, **122**, 5299–5310.

22 S. Gordon and J. McBride, Computer program for calculation of complex chemical equilibrium compositions and applications. I: Analysis, *NASA Ref. Pub.*, 1996, **19**, 1311.

23 M. W. Chase, J. L. Curnutt, J. R. Downey, R. A. McDonald, A. N. Syverud and E. A. Valenzuela, JANAF Thermochemical Tables, 1982 Supplement, *J. Phys. Chem. Ref. Data*, 1982, **11**, 695–940.

24 H. Werner and P. J. Knowles, A second order multiconfiguration SCF procedure with optimum convergence, *J. Chem. Phys.*, 1985, **82**, 5053–5063.

25 P. J. Knowles and H.-J. Werner, An efficient second-order MC SCF method for long configuration expansions, *Chem. Phys. Lett.*, 1985, **115**, 259–267.

26 H. Werner and W. Meyer, A quadratically convergent multiconfiguration selfconsistent field method with simultaneous optimization of orbitals and CI coefficients, *J. Chem. Phys.*, 1980, **73**, 2342–2356.

27 D. A. Kreplin, P. J. Knowles and H.-J. Werner, Second-order MCSCF optimization revisited. I. Improved algorithms for fast and robust second-order CASSCF convergence, *J. Chem. Phys.*, 2019, **150**, 194106.

28 H. Werner and P. J. Knowles, An efficient internally contracted multiconfiguration reference configuration interaction method, *J. Chem. Phys.*, 1988, **89**, 5803–5814.

29 P. J. Knowles and H.-J. Werner, An efficient method for the evaluation of coupling coefficients in configuration interaction calculations, *Chem. Phys. Lett.*, 1988, **145**, 514–522.

30 S. Langhoff and E. Davidson, Configuration Interaction Calculations on Nitrogen Molecule, *Int. J. Quantum Chem.*, 1974, **8**, 61–72.

31 T. H. Dunning, Gaussian basis sets for use in correlated molecular calculations. I. The atoms boron through neon and hydrogen, *J. Chem. Phys.*, 1989, **90**, 1007–1023.

32 H. J. Werner, P. J. Knowles, G. Knizia and F. R. Manby, *et al.*, M. S. MOLPRO, version 2019.1, a package of ab initio programs. 2019.

33 O. T. Unke and M. Meuwly, Toolkit for the Construction of Reproducing Kernel-Based Representations of Data: Application to Multidimensional Potential Energy Surfaces, *J. Chem. Inf. Model.*, 2017, **57**, 1923–1931.

34 G. Henkelman, B. Uberuaga and H. Jonsson, A climbing image nudged elastic band method for finding saddle points and minimum energy paths, *J. Chem. Phys.*, 2000, **113**, 9901–9904.

35 A. H. Larsen and J. J. Mortensen, The atomic simulation environment—a Python library for working with atoms, *J. Phys.: Condens. Matter*, 2017, **29**, 273002.

36 J. E. Bartmess, Negative Ion Energetics Data; NIST Chemistry Webbok, *NIST Standard Reference Database Number 69*, ed. P. J. Lindstrom and W. G. Mallard, National Institute of Standards and Technology, Gaithersburgh MD, 20899, 2001, http://webbook.nist.gov.

37 D. R. Lide, *Handbook of Chemistry and Physics*, Springer, US, 1992, pp. 10–211.

38 S. J. Cavanagh, S. T. Gibson, M. N. Gale, C. J. Dedman, E. H. Roberts and B. R. Lewis, High-resolution velocity-map-imaging photoelectron spectroscopy of the O(−) photodetachment fine-structure transitions, *Phys. Rev. A: At., Mol., Opt. Phys.*, 2007, **76**, 052708.

39 D. G. Truhlar and J. T. Muckerman, *Atom – Molecule Collision Theory*, ed. R. B. Bernstein, Springer, US, 1979, pp. 505–566.

3938 | *Phys. Chem. Chem. Phys.*, 2020, **22**, 3927–3939

This journal is © the Owner Societies 2020

40 N. E. Henriksen and F. Y. Hansen, *Theories of Molecular Reaction Dynamics*, Oxford, 2011.

41 D. Koner, L. Barrios, T. González-Lezana and A. N. Panda, State-to-State Dynamics of the Ne + HeH$^+$($\nu = 0, j = 0$) → NeH$^+$(ν', j') + He Reaction, *J. Phys. Chem. A*, 2016, **120**, 4731–4741.

42 D. Koner, R. J. Bemish and M. Meuwly, The C(^{3}P) + NO(X$^2\Pi$) → O(^{3}P) + CN(X$^2\Sigma^+$), N(^{2}D)/N(^{4}S) + CO(X$^1\Sigma^+$) reaction: Rates, branching ratios, and final states from 15 K to 20 000 K, *J. Chem. Phys.*, 2018, **149**, 094305.

43 L. Bonnet and J.-C. Rayez, Quasiclassical Trajectory Method for Molecular Scattering Processes: Necessity of a Weighted Binning Approach, *Chem. Phys. Lett.*, 1997, **277**, 183–190.

44 L. Bonnet and J.-C. Rayez, Gaussian Weighting in the Quasiclassical Trajectory Method, *Chem. Phys. Lett.*, 2004, **397**, 106–109.

45 J. D. Bender, P. Valentini, I. Nompelis, Y. Paukku, Z. Varga, D. G. Truhlar, T. Schwartzentruber and G. V. Candler, *J. Chem. Phys.*, 2015, **143**, 054304.

46 E. L. Kolsbjerg, M. N. Groves and B. Hammer, An automated nudged elastic band method, *J. Chem. Phys.*, 2016, **145**, 094107.

47 G. Knizia IboView: A program for chemical analysis, 2013.

48 R. A. Sultanov and N. Balakrishnan, Quantum mechanical investigations of the N(^{4}S) + O$_2$(X$^3\Sigma_g^-$) → NO(X$^2\Pi$) + O(^{3}P) reaction, *J. Chem. Phys.*, 2006, **124**, 124321.

49 F. Kaufman and L. J. Decker 7th Symp. (Int.) Combustion 1959, 57.

50 W. Wilson, Rate constant for the reaction N + O$_2$ → NO+ O, *J. Chem. Phys.*, 1967, **46**, 2017–2018.

51 J. B. Livesey, A. L. Roberts and A. Williams, The Formation of Oxides of Nitrogen in some Oxy-Propane Flames, *Combust. Sci. Technol.*, 1971, **4**, 9–15.

52 K. L. Wray and J. D. Teare, ShockTube Study of the Kinetics of Nitric Oxide at High Temperatures, *J. Chem. Phys.*, 1962, **36**, 2582–2596.

53 T. C. Clark, S. H. Garnett and G. B. Kistiakowsky, Reaction of Carbon Dioxide with Atomic Oxygen and the Dissociation of Carbon Dioxide in Shock Waves, *J. Chem. Phys.*, 1969, **51**, 2885–2891.

54 R. K. Hanson, W. L. Flower and C. H. Kruger, Determination of the Rate Constant for the Reaction O + NO → N + O$_2$, *Combust. Sci. Technol.*, 1974, **9**, 79–86.

55 A. Fernandez, A. Goumri and A. Fontijn, Kinetics of the Reactions of N(^{4}S) Atoms with O$_2$ and CO$_2$ over Wide Temperatures Ranges, *J. Phys. Chem. A*, 1998, **102**, 168–172.

56 R. K. Hansen and S. Salimian, in *Combustion Chemistry*, ed. W. C. Gardiner Jr., Springer, New York, NY, 1984, pp. 361–421.

57 I. D. Boyd and T. E. Schwartzentruber, *Nonequilibrium Gas Dynamics and Molecular Simulation*, Cambridge University Press, 2017.

58 J. C. Castro-Palacio, R. J. Bemish and M. Meuwly, Communication: Equilibrium rate coefficients from atomistic simulations: The O(^{3}P) + NO($^2\Pi$) → O$_2$(X$^3\Sigma_g^-$) + N(^{4}S) reaction at temperatures relevant to the hypersonic flight regime, *J. Chem. Phys.*, 2015, **142**, 091104.

59 A. Rahbee and J. J. Gibson, Rate constants for formation of NO in vibrational levels ν = 2 through 7 from the reaction N(^{4}S) + O$_2$ → NO$_+^+$ + O, *J. Chem. Phys.*, 1981, **74**, 5143–5148.

60 R. R. Herm, B. J. Sullivan and M. E. Whitson, Nitric oxide vibrational excitation from the N(^{4}S) + O$_2$ reaction, *J. Chem. Phys.*, 1983, **79**, 2221–2230.

61 G. E. Caledonia, R. H. Krech, D. B. Oakes, S. J. Lipson and W. A. M. Blumberg, Products of the reaction of 8 km s^{-1} N(^{4}S) and O$_2$, *J. Geophys. Res.*, 2000, **105**, 12833–12837.

62 M. V. Ivanov, R. Schinke and G. C. Mcbane, Theoretical investigation of vibrational relaxation of NO ($^2\Pi$), O$_2$($^3\Sigma_g^-$), and N$_2$($^1\Sigma_g^+$) in collisions with O(^{3}P), *Mol. Phys.*, 2007, **105**, 1183–1191.

63 R. P. Fernando and I. W. Smith, Vibrational relaxations of NO by atomic oxygen, *Chem. Phys. Lett.*, 1979, **66**, 218–222.

64 R. D. Sharma and R. G. Roble, Impact of the new rate coefficients for the O atom vibrational deactivation and photodissociation of NO on the temperature and density structure of the terrestrial atmosphere, *J. Geophys. Res.: Space Phys.*, 2001, **106**, 21343–21350.

65 M. Quack and J. Troe, Complex Formation in Reactive and Inelastic Scattering: Statistical Adiabatic Channel Model of Unimolecular Processes III, *Ber. Bunsenges. Phys. Chem.*, 1975, **79**, 170–183.

66 K. Glänzer and J. Troe, Vibrational relaxation of NO in collisions with atomic oxygen and chlorine, *J. Chem. Phys.*, 1975, **63**, 4352–4357.

67 H. V. Lilenfeld, *Deactivation of vibrationally excited NO and CO$_2$ by atoms,* Phillips Laboratory, Hanscom Air Force Base, Mass, 1994, PLTR942180, p. 24.

68 S. M. Anderson, F. S. Klein and F. Kaufman, Kinetics of the isotope exchange reaction of 18O with NO and O$_2$ at 298 K, *J. Chem. Phys.*, 1985, **83**, 1648–1656.

69 M. Meuwly and J. Hutson, Morphing ab initio potentials: A systematic study of Ne-HF, *J. Chem. Phys.*, 1999, **110**, 8338–8347.

This journal is © the Owner Societies 2020

Phys. Chem. Chem. Phys., 2020, **22**, 3927–3939 | 3939